This document is the unedited Author's version of a Submitted Work that was subsequently accepted for publication in *Nanoscale*, copyright © The Royal Society of Chemistry 2015 after peer review. To access the final edited and published work see https://pubs.rsc.org/en/content/articlelanding/2015/NR/C4NR05704J

Concave gold nanocubes assemblies as nanotraps for surface-enhanced Raman scattering-based detection of proteins

Paolo Matteini[1]*, Marella de Angelis[1], Lorenzo Ulivi[2], Sonia Centi[3], and Roberto Pini[1]

1. Institute of Applied Physics "Nello Carrara", National Research Council via Madonna del Piano 10, I-50019 Sesto Fiorentino, Italy
Fax: (+) 39 055 52256692 E-mail: p.matteini@ifac.cnr.it;
2. Institute for Complex Systems, National Research Council via Madonna del Piano 10, I-50019 Sesto Fiorentino, Italy
3. Department of Biomedical, Experimental and Clinical Sciences, University of Florence, viale Pieraccini 6, I-50139 Firenze, Italy

ABSTRACT

SERS detection of proteins is typically performed by using labeling agents with stable and high Raman scattering cross sections. This is a valuable approach for trace detection and quantification of a target protein but is unsuitable for inspecting its inherent structural and functional properties. On the other hand, direct SERS of proteins has been mainly devoted to the study of short peptides and aminoacidic sequences or of prosthetic groups with intense Raman signals, which is of scarce interest for a thorough characterization of most proteins. Here we try to overcome these limitations by setting-up an effective platform for the structural SERS analysis of proteins. The platform consists of an extended bidimensional array of gold concave nanocubes (CNCs) supported on a PDMS film. CNCs are close-packed through face-face and face-corner interactions generating a monolayered arrangement featuring well distributed nanoholes. Here protein molecules homogeneously experience an E-field enhancement outward from the metal surfaces surrounding it, which causes a large number of vibrations to be contemporary amplified. The proposed platform provides stable and detailed SERS spectra and confers rapidity and reproducibility to the analysis.

Introduction

Surface-enhanced Raman scattering (SERS) is a high-sensitivity vibrational spectroscopy technique with the potential to afford thorough information about the conformation and chemical structure of a target species.[1, 2] In this

respect, SERS represents a concrete possibility for the identification of biomolecules such as proteins at low concentrations as well as for the characterization of their structural organization and functional behavior.–
From a practical perspective, SERS detection requires that the molecular target come in close proximity (within a few nanometers from the metal surface) to an optical enhancer substrate based on plasmon nanostructures of noble metals such as gold or silver. Upon proper excitation of their plasmon resonances, the local electric field enhancement produces an increase in the Raman signal of the molecule by many orders of magnitude (typically in the $10^5 \div 10^7$ range).
To date, the most popular approach for the SERS detection of biomolecules rests on the use of colloidal metal nanospheres or spheroidal nanoparticles deposited on glass or silicon substrates or aggregated within salts-containing solutions or by means of narrow optofluidic channels. The 'hot spots' created at the gaps and junctions between two or multiple adjacent nanoparticles are at the basis of an amplified Raman signal. However, control over the hot spot distribution within these systems is intrinsically challenging, conferring scarce reproducibility and accuracy to the SERS analysis. Improved SERS performances can be obtained by replacing nanospheres with structures containing sharp nanoscaled corners and edges, due to their amplifying antenna-like behavior.[11, 12] These features provide the electromagnetic field enhancement with additional 2-3 orders of magnitude.[13, 14] In most recent literature, superstructures consisting of regular arrays of noble metal nanoparticles with different shapes and arrangement pattern have been introduced. In this case preformed colloids are chemically assembled to create large organized entities, which hold the promise of stronger and more reproducible SERS signals.
Currently, the most successful results of SERS analysis of proteins have been obtained by indirect methods that is by using labeling agents with stable and high Raman scattering cross sections.[4,19] These are valuable tools for trace detection and quantification of a biomolecular target but are unsuitable for inspecting its inherent structural and physiochemical properties. On the other hand, direct SERS of proteins has been mainly devoted to the study of short peptide fragments and aminoacidic sequences or of different prosthetic groups including those of heme- and flavo-proteins due to their strong SERS response. Nonetheless, this perspective restricts the investigation to very limited peptide sequences and appears of scarce interest for a thorough characterization of the protein . Other methods require that the protein is genetically modified with specific aminoacid motifs (e.g. the hexahistidine tag),[20, 24] which assure a successful binding of the biomolecule to the metal surface and thus the possibility to gain insights into its spectroscopic characterization, although at the expense of a sustainable practice.
In this paper we show how to overcome the limitations depicted above by setting-up an effective platform for the structural SERS detection of proteins. Our method escapes the needs of a preliminary modification of the biomolecule and confers rapidity and reproducibility to the analysis. Optimal results are achieved by the combination of two main factors: 1) the choice of nonspherical tipped metallic nanostructures with controlled architectural parameters and 2) their assembly into organized 2D-arrays featuring a distribution of nanoholes for protein entrapment and detection.

Results and Discussion

The SERS substrate herein engineered consists of an extended bidimensional array of gold concave nanocubes (CNCs) supported on a polydimethylsiloxane (PDMS) film. A scheme of the fabrication process is displayed in Fig. 1.
CNCs have been selected among other nanostructures due to a number of distinctive features including their intrinsically high SERS response and the availability of a solid surfactant-assisted synthesis protocol with high formation yields.[25, 26] We note that accessibility to colloidal batches with high monodispersity is essential for the preparation of large-area organized nanoparticle assemblies. In particular, particles of 130 nm size assured a >95% formation yield, as indicated by their sharp and intense plasmonic band (around 730 nm), which is not the case for the other sizes here tested (Fig. 2a). As a consequence, we focused on the former particle size for the following investigation. CNCs have a cube shape but with square pyramid-shaped depressions in each one of the six faces (Fig. 2b). The average angle between the facets of the concave cube and those of an ideal regular cube was determined to be 16° ± 1°, indicating that the facets of the CNCs are of high index {720} type, in accordance with previous literature. CNCs were obtained by a seed-mediated synthetic method including the use of cetyltrimethylammonium chloride (CTAC) surfactant as a stabilizing agent which plays an essential role in controlling the concave morphology of the final product.
Superstructures of CNCs were obtained by self-assembly of the nanoparticles at a hexane-water interface with alkanethiol in the organic phase (Figs. 3a,3b). In accordance with this procedure, destabilization of the colloidal particles is induced by the addition of ethyl alcohol, which triggers their adsorption at the interface. Here they undergo coating with alkanethiols, which succeed in converting the nanoparticle repulsive force into van der Waals interactions and subsequent particles packing. After evaporation of both solvents, the as-formed gold islands are easily adhered to a PDMS film, conferring it a mirror-like metallic sheen (Fig. 3c). The CNCs are close-packed in a monolayer through face-face and face-corner interactions featuring well distributed holes of nanometric size (Fig. 3b). These act as nanotraps for accommodating the target protein once its pristine solutions are sandwiched and left dry between the SERS substrate and a flat and chemically-inert Teflon substrate. PDMS and Teflon generate a twofold water-repulsive interface that force protein to preferentially interact with the gold surface during the water evaporation process. At the same time this procedure assures a more homogeneous distribution of the protein over the SERS substrate with respect to methods based on simple drop coating deposition[36] (Fig. S1). The optical coupling between the plasmon bands of the particles is responsible for a broad surface plasmon peak centered at 640 nm (Fig. 3d). The rate of alkanethiol coating rules the compactness of the final nanoparticles assembly,[31] which is obtained in the form of loose to dense monolayer and eventually leads to the formation of disordered 3D aggregates (Fig. S2). Accordingly, an increase in the absorbance due to a significant decrease in the void areas and an increase in plasmon coupling is observed upon rising the thiol concentration up to 10^{-6} M (Fig. 3d). The transition from 2-dimensional

arrays to aggregated clusters occurring at higher thiol concentrations is instead responsible for a remarkable decrease and broadening in their absorption curves, which can be attributed to multiple plasmon coupling effects (Fig. 3d). After the gold assembly is formed and adhered to the PDMS film, it was subjected to alkaline oxidizing treatment, then cleansed in methanol and finally plasma etched, which succeeded in removing the alkanethiol from the metal surfaces (Fig. S3).
The measured enhancement factor (EF) of the SERS substrate at the optimal thiol concentration of 1 10^{-6} M is on the order of ~10^{6} (see Supplementary Information and Fig. S4) based on a minimum of 30 measurements on 4 replica substrates. Interestingly, our EF value is in line with values previously observed in superstructured systems based on lithographed or template-assisted[38] gold nanoscale building blocks, which is not trivial when dealing with self-assembled substrates from colloidal particles. A visual appearance of the SERS response at a microscopic scale is here provided by mapping the signal from a probe molecule over (30 × 30) μm^2 areas (Fig. S5). The homogeneity of the measured signal, which is quantified by a relative standard deviation of 20%, suggests a rather regular disposition of the hot spots throughout the SERS substrate.
The nanoscale distribution of the electric-field enhancement was simulated with a finite element method (FEM).[18, 39] As anticipated, the close assembly of the concave nanocubes was responsible for the formation of nanoholes at the interface between adjacent particles. Specifically, theoretical calculations evidenced that two main sites can be responsible for substantial SERS activity (Fig. 4): the junction points between cube corners (Fig. 4a) or between a cube corner and the face of an adjacent cube (Fig. 4b), and the nanoholes (Figs. 4a,c). The former type sites show 10-100 times larger E-field intensities with respect to those simulated within the nanoholes. Considering that the surface for analyte adsorption provided by the latter is quite larger with respect to that available at the junction points formed by the corners, we deduce that the nanoholes will mainly contribute to the final performances of our SERS substrate. Interestingly, the most effective configuration among those considered corresponded to three nanocubes in a shifted array (a cube with its corners approximating the middle of each adjacent cube face). While large E-field intensity values are generated at nearly the entire interface between particles, we may observe that this configuration appears less frequently in our substrate (Fig. 3a) and is thus expected to contribute to a lesser extent to the whole system efficiency.

The SERS substrate was finally tested for the detection of two proteins, i.e. insulin and cytochrome c, which are low-abundance biomarkers of principal biological processes such as the control of physiological glycometabolism and the incurrence of malignant tumors and fulminant hepatitis, respectively. Apart from the advantages offered by SERS in the ultrasensitive and effective identification of these proteins, SERS detection is expected to offer rich insights into tracking their functionality in respect to their secondary structure and conformational states. Nonetheless, the SERS analysis of these proteins has been previously proved challenging. First, large differences of peak intensity and dramatic frequency changes in the SERS spectra of insulin have been reported when it was detected in aggregating mixtures of metal colloids.[40, 41] These effects can be ascribed to the combination of an uneven hot

spot distribution and the variability in the interactions established by the molecule with the colloidal surface, which similarly affected the signal of other biological species on SERS substrates with an uncontrolled particles assembly.[7, 20, 42, 43] Another matter requiring careful scrutiny is the SERS detection of heme-proteins like cytochrome c. In these cases, the intense SERS signals of the heme group are responsible for masking the spectral features of the remaining protein parts, in spite of using a nonresonant excitation.[44, 45]

Representative spectra of insulin and cytochrome c are reported in Fig. 5 along with the background signal of the SERS substrate. In both cases we fixed the excitation wavelength to 639 nm in an attempt to maximize the SERS signal thanks to an excellent overlap with the plasmonic band originated by the CNCs array (Fig. 3d). The SERS spectrum of insulin provides abundant and characteristic information including the band at 624 cm^{-1} assigned to Phe, the pair of Tyr Raman markers at 830 and 866 cm^{-1}; the C-C stretching mode at 950 cm^{-1}; Phe ring breathing modes at 1003 and 1030 cm^{-1}; Tyr and Phe peaks at 1181 and 1208 cm^{-1}; amide III band at 1270 cm^{-1}; -CH deformation modes at 1365 and 1385 cm^{-1} and a –CH2 deformation mode at 1450 cm^{-1}.[9, 41] The group of peaks between 1500 and 1615 cm^{-1} can be ascribed to the Phe, Tyr and Trp modes of the aromatic ring, while amide I band appears at 1642 cm^{-1}. The presence of this band is regarded as fundamental for assigning the secondary structure being it dependent on the conformation of the polypeptide backbone and on the presence of intra- and inter- molecular hydrogen bonds.[46] Additionally, our results indicated a low variability in the SERS spectra of insulin by sequential measurements from different locations and replica substrates (Fig. S6).

Analogously to the case of insulin, the nonresonant SERS spectrum of cytochrome C provided extensive vibrational information. In this case frequencies not merely associated with the heme group but originated by some amino acid residues and the peptide backbone were detected. Here the typical vibrational modes of heme are apparent: ν_{10} (1633 cm^{-1}, B1g), ν_{11} (1540 cm^{-1}, B1g), ν_{13} (1230 cm^{-1}, B1g), ν_{15} (746 cm^{-1}, B1g), ν_{22} (1124 cm^{-1}, A2g), ν_{30} (1164 cm^{-1}, B2g), ν_4 (1370 cm^{-1}/1366 cm^{-1}, A1g).[21, 44] In addition, some bands can be ascribed to different aminoacid residues: e.g. 1555 cm^{-1} and 880 cm^{-1} (Trp), 1000 cm^{-1} and 1030 cm^{-1} (Phe), and 840 cm^{-1} and 860 cm^{-1} (Tyr); while the 1240 cm^{-1} mode is attributed to the amide III band and the 1447 cm^{-1} to the CH_2 deformation.[33, 47]

The suppression of some bands (such as the above-mentioned amide I band) and the fluctuation in the SERS response of various proteins from different locations of the SERS substrate have been frequently reported in the literature.[35, 40, 42, 43] These have been mostly interpreted as the consequence of the distancing of the protein with respect to the metal surface.[48, 49] In this case, a partial to full amplification of some frequencies at the expense of those generated by bonds placed at a larger distance from the surface of the SERS substrate is expected to occur. On the contrary we observed stable and detailed SERS spectra, which require a different interpretation. We may speculate that, once entrapped within a nanohole, the protein molecule homogeneously experiences an E-field enhancement outward from the metal surfaces surroundings it, which causes a larger number of vibrations to be contemporary amplified (Fig. 6). Obviously, the more regular is the hot spots (and nanoholes) distribution, the larger will be the influence of this effect over

the final protein spectrum. Similar arguments can be used to explain the appearance of some non-heme vibrational modes in the cytochrome c spectrum. Again, the SERS active surfaces enclosing the molecule can induce an addictive effect to modes generated by peripheral parts of the protein that are typically shielded by more effective heme modes.
In conclusion we described an original strategy for the SERS detection of proteins based on a powerful SERS substrate that is composed of a 2D-distribution of gold nanocrystals. The peculiar characteristics of these nanocrystals and their assembly into organized arrays favored the formation of nanoscaled holes, which play the role of traps for effective protein detection. These features conferred to our SERS substrate solidity and reliability, which offered the possibility to unveil a number of structural characteristics of a protein by a simple and rapid procedure. We may envision a number of future applications in the biological and medical areas for the proposed SERS system including the study of protein-ligand and protein-drug interactions and the identification of physiological mechanisms behind several pathological conditions.

Experimental

Materials. Reagents, metallic salts and other analytical grade chemicals were acquired from Sigma-Aldrich or Merck. Polydimethylsyloxane (PDMS) was obtained from Sylgard. Human insulin solution (10 g L^{-1} in pH 8.2 HEPES) and cytochrome c from bovine hearth were obtained from Sigma and used as received.

Concave gold nanocubes synthesis. The particles were synthesized in accordance with the procedure of Zhang *et al.* with slight modifications. In brief, gold seeds were prepared by quickly injecting 0.3 mL of ice-cold $NaBH_4$ (10 mM) into a rapidly stirred solution containing 0.125 mL $HAuCl_4$ (10 mM) and 5 mL of cetyltrimethylammonium chrloride (CTAC) (100 mM). After 2 hours without agitation, the seed solution was 1000-fold diluted with 0.1 M CTAC through two consecutive steps. CNCs were obtained by slowly adding 0.4 mL of the diluted seeds to a rapidly stirred growth solution containing 40 mL of CTAC (100 mM), 2 mL $HAuCl_4$ (10 mM), 0.4 mL $AgNO_3$ (10 mM), 0.6 mL HCl (1 M) and 0.4 mL of ascorbic acid (100 mM). The solution was left undisturbed overnight, then centrifuged (3×, 1000 g', 40 min) and finally 4-fold concentrated and stored in cetylpyridinium chloride (CPC, 10 mM) until further use. Nanocrystal dimensions were obtained by dynamic light scattering (DLS) measurements on a Malvern Nano ZS90. TEM micrographs of the particles were acquired with a Philips CM-12 microscope running at 100 kV. The optical properties of CNCs were characterized by using a Jasco V-560 spectrophotometer.

PDMS film fabrication. For the fabrication of PDMS circular films (0.8 cm diameter, 200 µm thickness), 50 µL of 10:1 base to curing agent mixture (Sylgard 184) were poured into 0.5 cm^2 polystyrene circular molds and cured over a 40 °C hot plate. Just before use, a plastic cylinder (5 cm length × 1 cm diameter) was gently pressed over the air-exposed side of the film while the

other side (protected from air) was used for capturing the floating gold islands.

Nanocrystal array fabrication. The assembly of the nanoparticles into organized arrays was pursued by following previous protocols with some modifications. 0.08 mL of the nanoparticle colloid was deposited on the bottom of a PTFE cell (5 cm^2 area) to which 0.4 mL of *n*-hexane containing different concentrations of 1-dodecanthiol were added. 0.16 mL of EtOH was then dropped (at about 0.01 mL s^{-1}) to the top of the hexane phase, leading to the assembly of gold nanoparticles at the water/hexane interface. The floating gold island was adhered to the PDMS film upon complete evaporation of hexane. The PDMS-supported gold substrates were then soaked in a mixture of NH_4OH-H_2O_2-H_2O at 1:1:61 volume ratio and 40 °C for 30 min,[53] followed by sonication in methanol at 30 °C for 15 min and oxygen plasma treatment (Harrick Scientific Corp., PDC-002 operated at 60 Hz and 0.2 Torr air) for 4 minutes. The optical properties of CNCs arrays were characterized by a portable spectrometer (EPP2000 by Stellarnet Inc.) and a Shimadzu 8300 ATR-FTIR spectrophotometer. The fluorescence distribution of anti-rabbit IgG-FITC protein over the gold substrate was obtained with a Leica DMI3000B microscope.

Surface-Enhanced Raman Scattering spectroscopy. SERS experiments were conducted in a micro-Horiba XPlora system. The spectrograph uses a 1200 grooves mm^{-1} grating with a confocal microscope in backscattering geometry and a 2D-CCD camera. We used a 50× objective with a NA value of 0.5, accumulation times of 5 s/spectrum and a ~70 μW power on the sample. Typically, for a single SERS measurement, we used 10 μL of fresh 2 10^{-6} M and 17 10^{-6} M solutions of cytochrome c and insulin in Milli-Q water, respectively. For each sample, the measurement was conducted on at least 3 replica substrates obtained in the same experimental conditions. All data were baseline corrected when needed. The samples were prepared according to Fig. 1. Methods used for FEM modeling and EF calculation are described in Supporting Information.

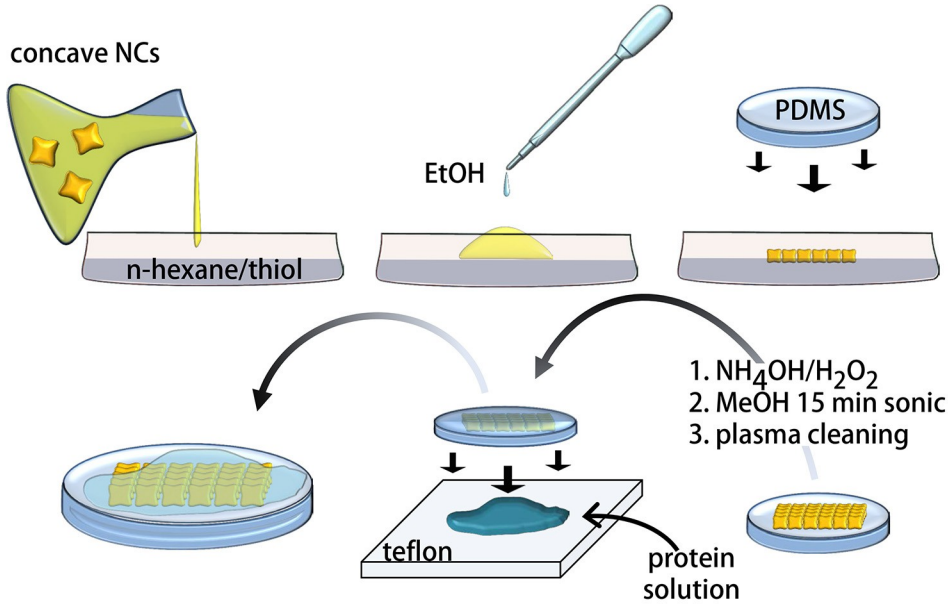

Fig. 1. Scheme of the fabrication of the CNCs arrays, their immobilization over PDMS films and preparation of the protein samples for SERS analysis .

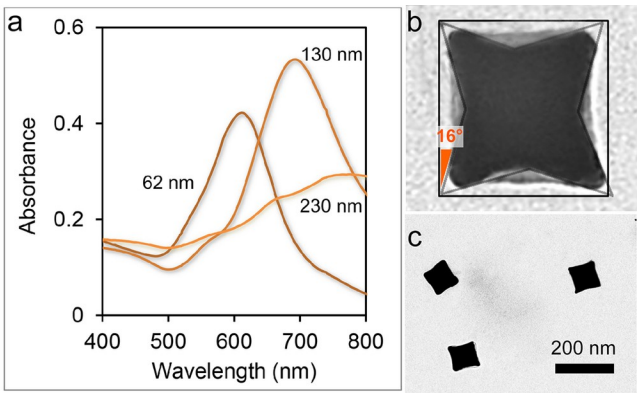

Fig. 2. (a) Change in the optical properties of colloidal solutions of gold CNCs with different sizes. (b) TEM magnification of a CNC: the angle between the facets of the cube and of the (100) facets of an ideal cube were 16° on average. (c) TEM micrograph of 130 nm-sized CNCs.

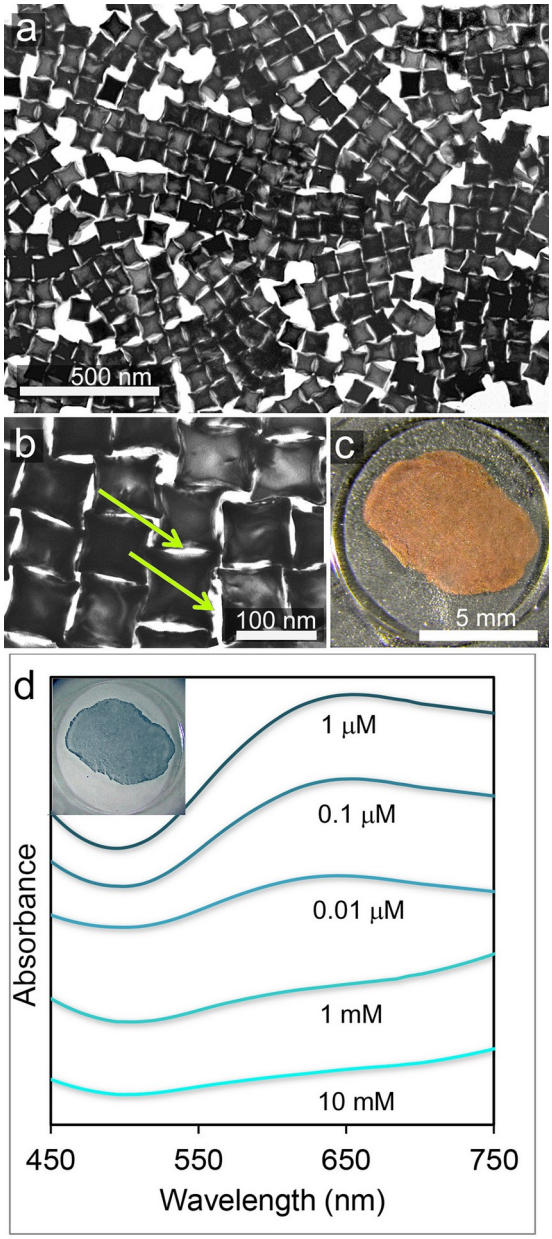

Fig. 3. TEM image (a) and zoomed-in image (b) of a representative CNCs array. Nanoholes are indicated with arrows. (c) Visual appearance of a CNCs array over a PDMS film. (d) Absorbance spectra of CNCs-PDMS substrates prepared by using a different concentration of alkanethiol in the 0.01 μM ÷ 10 mM range. Inset: transmitted light microscopy image of the substrate visualized in (c).

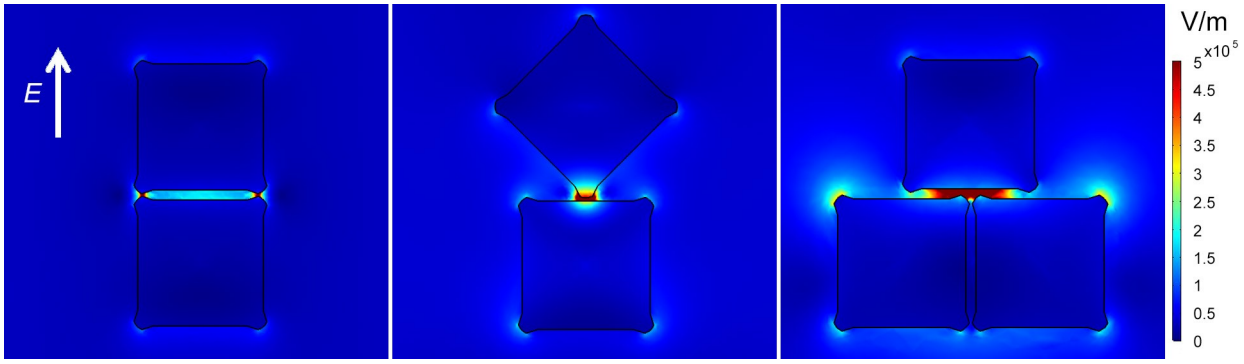

Fig. 4. Simulated norm of the electric field for different gold CNCs assemblies: a) two nanocubes with parallel faces, b) two nanocubes with the corner of one cube facing the face of another one, c) three nanocubes in a shifted array.

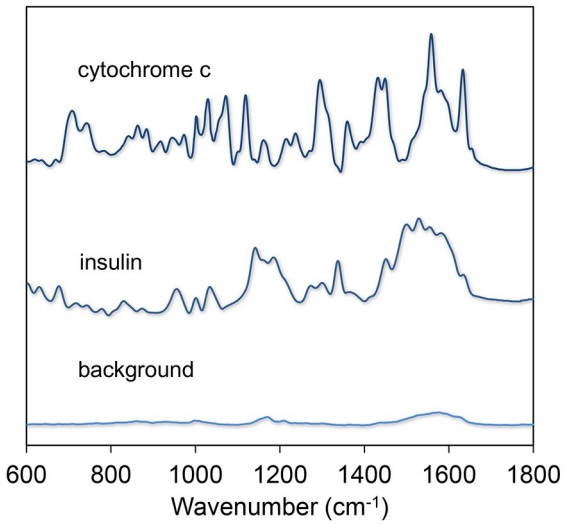

Fig. 5. SERS spectra of cytochrome c and insulin obtained with a laser excitation of 639 nm and an acquisition time of 5 s. The background signal (before deposition of the protein) is visualized on the bottom of the graph.

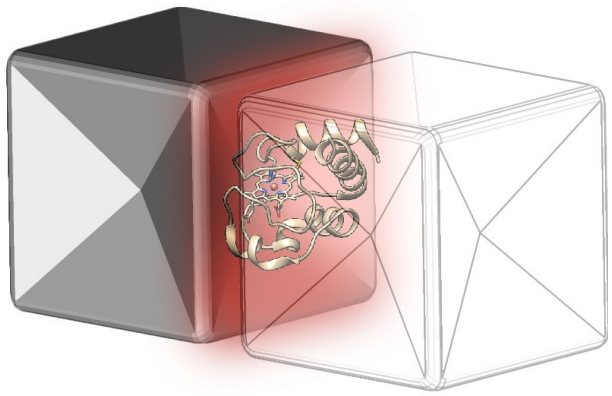

Fig. 6. Once entrapped in a nanohole between assembled CNCs, the protein (cytochrome c in the example) experiences an homogeneous SERS effect, which is expected to amplify vibrational modes of a large part of the protein and ultimately to improve the detail and reproducibility of its SERS spectrum (protein and CNCs are not to scale).

Supplementary Information

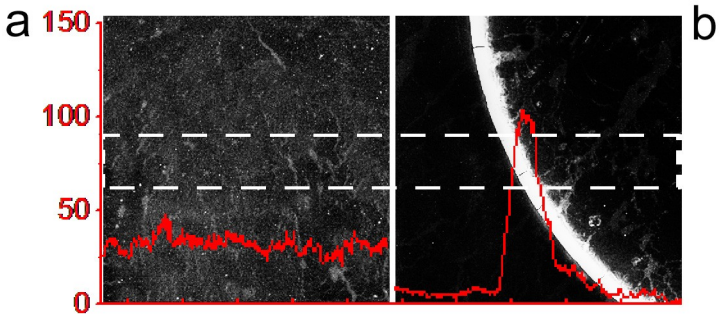

Fig. S1. Fluorescence images (λ_{ex} = 488 nm, 2×2 mm^2) of anti-rabbit IgG-FITC (10 µL, 2 10^{-6} M) deposited over a CNCs-PDMS substrate according to the procedure described in Fig. 1 (a) and by drop deposition (b). The fluorescence intensity profile (red line, left y-axis, a.u.) of the protein averaged over the rectangular selection (indicated with a dashed line) is superimposed. The fluorescence signal is essentially constant throughout the sample when procedure (a) is used while is mainly localized at the edge of the dried drop and very low inside in the case of procedure (b).

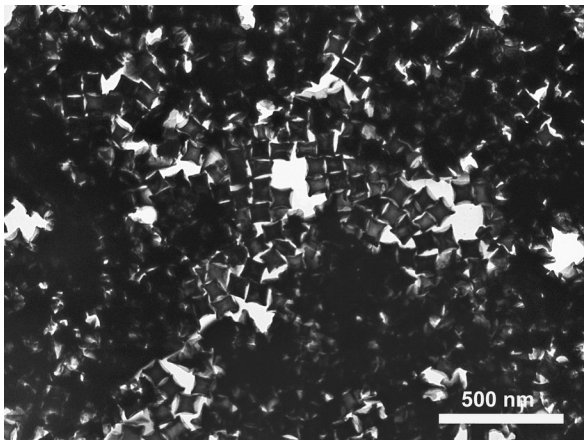

Fig. S2. TEM image of CNCs assembled by using 1 mM alkanethiol.

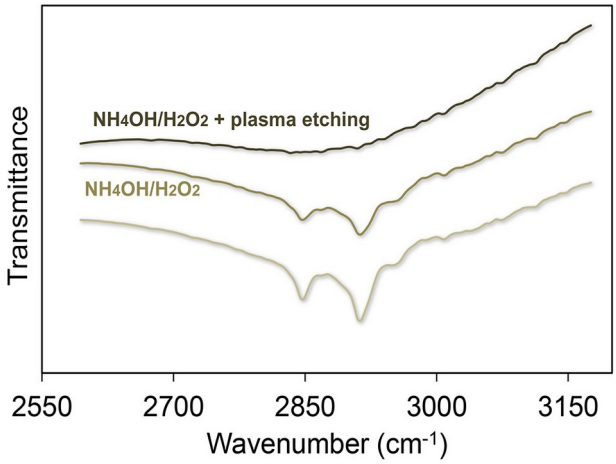

Fig. S3. ATR-FTIR spectra of CNCs-PDMS substrates: as-prepared (bottom), after the alkaline oxidizing treatment (middle) and further plasma oxygen cleaning (top). The disappearance of the 2846 and 2916 cm^{-1} bands assigned to the symmetric and asymmetric stretching CH_2 vibrations of the alkanethiol chain [A.N. Parikh and D.L. Allara, *J. Chem. Phys.* 1992, **96,** 927-945] suggests its complete removal [D.J. Kim, R. Pitchimani, D.E. Snow, L.J. Hope-Weeks, *Scanning*, 2008, **30,** 118-122] from the gold surface once the treatment was completed.

Calculation of the Enhancement Factor

The enhancement factor (EF) has been determined by comparing the 1594 cm^{-1} band intensity of the SERS spectrum (I_{SERS}) of 4-methylbenzenethiol (MBT) molecules deposited on CNCs substrates with that of the Raman measurement (I_R) of solid MBT. We have used the definition for the average SERS EF on substrates given by Le Ru *et al.* [E.C. Le Ru, E. Blackie, M. Meyer, P. G. Etchegoin, *J. Phys. Chem. C*, 2007, **111,** 13794-13803]:

$$\mathrm{EF}=\frac{I_{\mathrm{SERS}}/N_{\mathrm{Surf}}}{I_R/N_{\mathrm{Vol}}}, \qquad (1)$$

Where N_{Surf} is the average number of adsorbed molecules in the scattering volume (i.e. at the SERS surface) for the SERS experiment, N_{vol} is the average number of molecules in the scattering volume for the Raman measurement.
For the SERS measurement we assume the substrate consisting of a repeating pattern metallic structures and the irradiated area much larger than the individual structures forming the substrate. Let $\mu_M[m^{-2}]$ be the surface density of the individual nanostructures with respect to the main plane forming the substrate, and A_M the metallic surface area in each structure. Assuming a surface density of molecules $\mu_S[m^{-2}]$ on the metal (with footprint f_p being its reciprocal), if A_{eff} is the effective surface area of the scattering volume, we can define $N_{Surf} = \mu_M A_M \mu_S A_{eff}$. On the other hand if c_R is the average number of molecules per unit volume $N_{Vol} = c_R V = c_R H_{eff} A_{eff}$, where H_{eff} is the effective height of the scattering volume. Eq. (1) reduces to:

$$\mathrm{EF}=\frac{I_{\mathrm{SERS}}/\mu_M A_M \mu_S}{I_R/c_R H_{\mathrm{eff}}}, \qquad (1)$$

where the parameter H_{eff} , enables the connection between the 2D and 3D measurement. In the case of a complete coverage of the surface under illumination by CNCs, $\mu_M A_M$ is 1, and

$$\mathrm{EF}=\frac{I_{\mathrm{SERS}}}{I_R} f_p c_R H_{\mathrm{eff}}, \qquad (1)$$

Solid MBT (~53 10^{20} molecules per cm^3) was used for the evaluation of I_R. H_{eff} was measured (34 µm) according with the procedure described in Cai *et al.* [W.B. Cai, B. Ren, X.Q. Li, C.X. She, F.M. Liu, X.W. Cai, *Surf. Sci.*, 1998, **406,** 9-23]. f_p was assumed = 0.19 nm^2/molecule according to Rycenga *et al.* [M. Rycenga, X.H. Xia, C.H. Moran, F. Zhou, D. Qin, Z.Y. Li, Y.A. Xia, *Angew. Chem. Int. Edit.*, 2011, **50**, 5473-547]. In our experimental conditions, we measured a SERS signal ~100 times larger than the Raman one (Fig. S4), therefore we estimated an EF ~ 10^6. .

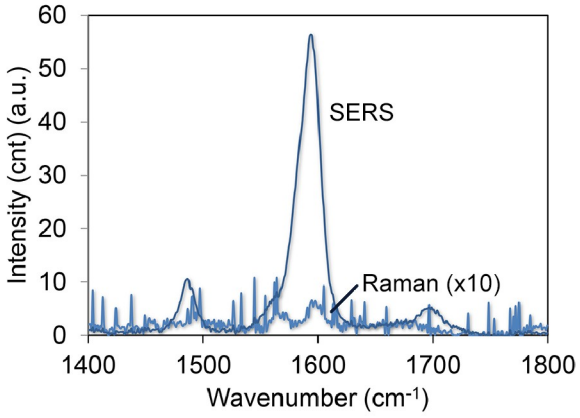

Fig. S4. Comparison between the 1594 cm^{-1} Raman and SERS bands of MBT.

Finite Element Method modeling

Simulation of the electric field has been performed using a finite element method (FEM). We realized our finite element models using the commercial software Comsol Multiphysics 4.4 in the scattering mode of the wave-optics-module to solve the Helmholtz equation. By normalizing the incident electric field we can observe the local field enhancement factor directly in form of the normalized electric field.

Our geometry is composed of several gold concave nanocubes with 100 nm size surrounded by air. We have considered three different mutual positions of the CNCs that are the most representative of the actual nanoparticle assembly as shown in the TEM images of Fig. 3. This choice represents a compromise between calculation domain size and solving time. The gold-to-gold gap distance is set to 1 and 0 nm for the face-to-face and face-to-corner configurations, respectively. The metal is described through its measured

dielectric function [P.B. Johnson & R.W. Christy, *Phys. Rev. B*, 1972, **6,** 4370-4379]. The domains are delimited by perfectly matched layers (PML) in order to reach perfect absorption at the outer boundaries. All the simulation are done in 3D and the incident field is assumed to be an electromagnetic plane wave with linear polarization and 639 nm wavelength. Our experimental setup is with light at normal incidence onto the layer of nanocubes (light propagating along the z axis) and polarization along the y direction (see Fig. 4).

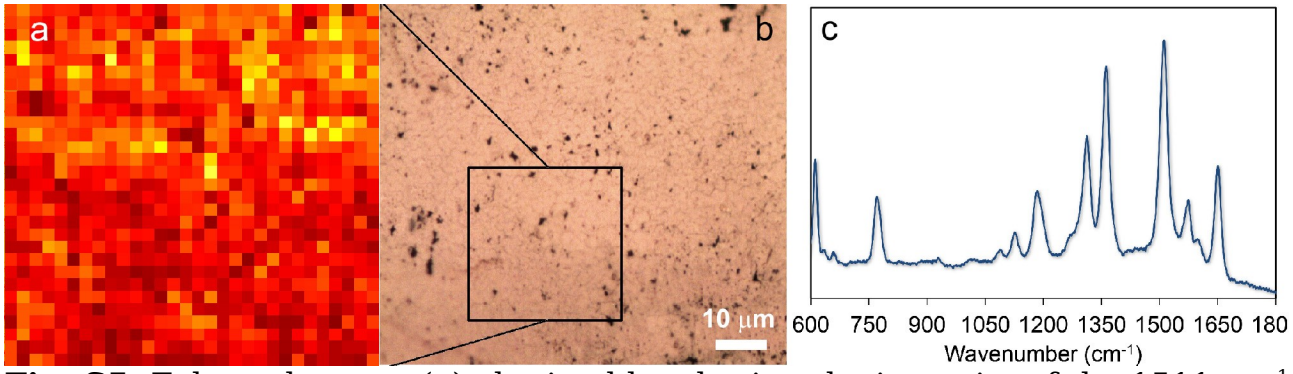

Fig. S5. False-color map (a) obtained by plotting the intensity of the 1511 cm^{-1} Raman band of SERS spectra of Rhodamine 6G (a representative SERS spectrum is visualized in (c)) measured over a 30×30 μm^2 area with a resolution of 1×1 μm^2 of a CNCs-PDMS substrate as identified in the back-reflection image (b). The sample was prepared as described in the Methods section for protein samples and schematized in Fig. 1. A solution of Rhodamine 6G 1 10^{-6} M was used for the measurement.

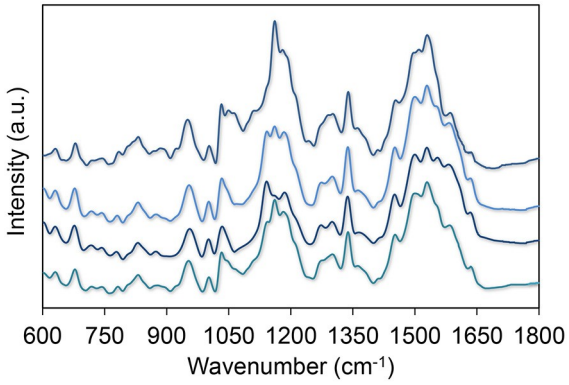

Fig. S6. Examples of SERS spectra of insulin taken from random locations of a CNCs-PDMS substrate.

Acknowledgments

This work has been partially supported by Regione Toscana and European Community within the frame of the ERANET+ Project “BI-TRE – Biophotonic Technologies for Tissue Repair ”

References

1 K. A. Willets and R. P. Van Duyne, *Annu Rev Phys Chem*, 2007, **58**, 267-297.
2 M. Moskovits, *Rev. Mod. Phys.*, 1985, **57**, 783-826.
3 D. A. Stuart, A. J. Haes, C. R. Yonzon, E. M. Hicks and R. P. Van Duyne, *IEE proceedings. Nanobiotechnology*, 2005, **152**, 13-32.
4 R. A. Alvarez-Puebla and L. M. Liz-Marzan, *Small*, 2010, **6**, 604-610.
5 D. Cialla, S. Pollok, C. Steinbrücker, K. Weber and J. Popp, *Nanophotonics*, 2014, DOI: DOI: 10.1515/nanoph-2013-0024, 1-30.
6 K. Saha, S. S. Agasti, C. Kim, X. Li and V. M. Rotello, *Chemical reviews*, 2012, **112**, 2739-2779.
7 C. Blum, T. Schmid, L. Opilik, S. Weidmann, S. R. Fagerer and R. Zenobi, *J Raman Spectrosc*, 2012, **43**, 1895-1904.
8 M. Wang, N. Jing, I. H. Chou, G. L. Cote and J. Kameoka, *Lab Chip*, 2007, **7**, 630-632.
9 V. P. Drachev, M. D. Thoreson, E. N. Khaliullin, V. J. Davisson and V. M. Shalaev, *J Phys Chem B*, 2004, **108**, 18046-18052.
10 P. H. C. Camargo, M. Rycenga, L. Au and Y. N. Xia, *Angew Chem Int Edit*, 2009, **48**, 2180-2184.
11 L. Rodriguez-Lorenzo, R. A. Alvarez-Puebla, F. J. G. de Abajo and L. M. Liz-Marzan, *J Phys Chem C*, 2010, **114**, 7336-7340.
12 J. P. Xie, Q. B. Zhang, J. Y. Lee and D. I. C. Wang, *Acs Nano*, 2008, **2**, 2473-2480.
13 P. S. Kumar, I. Pastoriza-Santos, B. Rodriguez-Gonzalez, F. J. Garcia de Abajo and L. M. Liz-Marzan, *Nanotechnology*, 2008, **19**.
14 S. Y. Lee, L. Hung, G. S. Lang, J. E. Cornett, I. D. Mayergoyz and O. Rabin, *Acs Nano*, 2010, **4**, 5763-5772.
15 P. N. Sisco and C. J. Murphy, *J Phys Chem A*, 2009, **113**, 3973-3978.
16 C. Fang, D. Brodoceanu, T. Kraus and N. H. Voelcker, *Rsc Adv*, 2013, **3**, 4288-4293.
17 Z. N. Zhu, H. F. Meng, W. J. Liu, X. F. Liu, J. X. Gong, X. H. Qiu, L. Jiang, D. Wang and Z. Y. Tang, *Angew Chem Int Edit*, 2011, **50**, 1593-1596.
18 M. Alba, N. Pazos-Perez, B. Vaz, P. Formentin, M. Tebbe, M. A. Correa-Duarte, P. Granero, J. Ferre-Borrull, R. Alvarez, J. Pallares, A. Fery, A. R. de Lera, L. F. Marsal and R. A. Alvarez-Puebla, *Angew Chem Int Edit*, 2013, **52**, 6459-6463.
19 X. X. Han, B. Zhao and Y. Ozaki, *Anal Bioanal Chem*, 2009, **394**, 1719-1727.
20 G. V. P. Kumar, B. A. A. Reddy, M. Arif, T. K. Kundu and C. Narayana, *J Phys Chem B*, 2006, **110**, 16787-16792.
21 I. Delfino, A. R. Bizzarri and S. Cannistraro, *Biophys Chem*, 2005, **113**, 41-51.
22 N. S. Lee, Y. X. Hsieh, M. D. Morris and L. M. Schopfer, *J. Am. Chem. Soc.*, 1987, **109**, 1358-1363.
23 T. M. Cotton, S. G. Schultz and R. P. Van Duyne, *J. Am. Chem. Soc.*, 1980, **102**, 7960-7962.
24 R. Ahijado-Guzman, P. Gomez-Puertas, R. A. Alvarez-Puebla, G. Rivas and L. M. Liz-Marzan, *Acs Nano*, 2012, **6**, 7514-7520.
25 J. A. Zhang, M. R. Langille, M. L. Personick, K. Zhang, S. Y. Li and C. A. Mirkin, *J Am Chem Soc*, 2010, **132**, 14012-14014.

26 M. Rycenga, M. R. Langille, M. L. Personick, T. Ozel and C. A. Mirkin, *Nano Lett*, 2012, **12**, 6218-6222.
27 C. B. Murray, C. R. Kagan and M. G. Bawendi, *Annu Rev Mater Sci*, 2000, **30**, 545-610.
28 Y. Yu, Q. B. Zhang, X. M. Lu and J. Y. Lee, *J Phys Chem C*, 2010, **114**, 11119-11126.
29 F. Reincke, S. G. Hickey, W. K. Kegel and D. Vanmaekelbergh, *Angew Chem Int Edit*, 2004, **43**, 458-462.
30 H. W. Duan, D. Y. Wang, D. G. Kurth and H. Mohwald, *Angew Chem Int Edit*, 2004, **43**, 5639-5642.
31 Y. K. Park, S. H. Yoo and S. Park, *Langmuir*, 2007, **23**, 10505-10510.
32 M. J. Allen, V. C. Tung, L. Gomez, Z. Xu, L. M. Chen, K. S. Nelson, C. W. Zhou, R. B. Kaner and Y. Yang, *Adv Mater*, 2009, **21**, 2098-2102.
33 M. Kahraman, B. N. Balz and S. Wachsmann-Hogiu, *Analyst*, 2013, **138**, 2906-2913.
34 P. Matteini, L. G. Dei, E. Carretti, N. Volp, A. Goti and R. Pini, *Biomacromolecules*, 2009, **10**, 1516-1522.
35 S. Keskin and M. Culha, *Analyst*, 2012, **137**, 2651-2657.
36 J. Filik and N. Stone, *Analyst*, 2007, **132**, 544-550.
37 C. David, N. Guillot, H. Shen, T. Toury and M. L. de la Chapelle, *Nanotechnology*, 2010, **21**.
38 C. Farcau and S. Astilean, *J Phys Chem C*, 2010, **114**, 11717-11722.
39 P. Matteini, F. Tatini, L. Luconi, F. Ratto, F. Rossi, G. Giambastiani and R. Pini, *Angew Chem Int Edit*, 2013, **52**, 5956-5960.
40 D. Kurouski, T. Postiglione, T. Deckert-Gaudig, V. Deckert and I. K. Lednev, *Analyst*, 2013, **138**, 1665-1673.
41 D. Kurouski, M. Sorci, T. Postiglione, G. Belfort and I. K. Lednev, *Biotechnol Progr*, 2014, **30**, 488-495.
42 S. Stewart and P. M. Fredericks, *Spectrochim Acta A*, 1999, **55**, 1615-1640.
43 X. M. Dou, Y. M. Jung, Z. Q. Cao and Y. Ozaki, *Appl Spectrosc*, 1999, **53**, 1440-1447.
44 G. Niaura, A. K. Gaigalas and V. L. Vilker, *J Electroanal Chem*, 1996, **416**, 167-178.
45 X. X. Han, G. G. Huang, B. Zhao and Y. Ozaki, *Anal Chem*, 2009, **81**, 3329-3333.
46 D. Kurouski, T. Deckert-Gaudig, V. Deckert and I. K. Lednev, *J Am Chem Soc*, 2012, **134**, 13323-13329.
47 F. Wei, D. M. Zhang, N. J. Halas and J. D. Hartgerink, *J Phys Chem B*, 2008, **112**, 9158-9164.
48 C. D. Keating, K. M. Kovaleski and M. J. Natan, *J Phys Chem B*, 1998, **102**, 9404-9413.
49 K. Kneipp, H. Kneipp, I. Itzkan, R. R. Dasari and M. S. Feld, *J Phys-Condens Mat*, 2002, **14**, R597-R624.
50 Q. Ye, J. X. Fang and L. Sun, *J Phys Chem B*, 1997, **101**, 8221-8224.
51 J. Gersten and A. Nitzan, *J. Chem. Phys.*, 1980, **73**, 3023-3037.
52 C. A. Murray and D. L. Allara, *J. Chem. Phys.*, 1980, **76**, 1290-1303.
53 D. J. Kim, R. Pitchimani, D. E. Snow and L. J. Hope-Weeks, *Scanning*, 2008, **30**, 118-122.